

See discussions, stats, and author profiles for this publication at: <https://www.researchgate.net/publication/231704745>

Transient Microstructure of Low Hard Segment Thermoplastic Polyurethane under Uniaxial Deformation

ARTICLE *in* MACROMOLECULES · JUNE 2008

Impact Factor: 5.8 · DOI: 10.1021/ma800306z

CITATIONS

45

READS

20

3 AUTHORS, INCLUDING:



[Hilmar Koerner](#)

Wright-Patterson Air Force Base

154 PUBLICATIONS **2,722** CITATIONS

[SEE PROFILE](#)



[John Kelley](#)

Wright-Patterson Air Force Base

3 PUBLICATIONS **87** CITATIONS

[SEE PROFILE](#)

Transient Microstructure of Low Hard Segment Thermoplastic Polyurethane under Uniaxial Deformation

Hilmar Koerner,^{*,†,‡} John J. Kelley,[†] and Richard A. Vaia[†]

Materials and Manufacturing Directorate, Air Force Research Laboratory, AFRL/RXBP, 2941 Hobson Way, Wright-Patterson AFB, Ohio 45433, and Universal Technology Corporation, Dayton, Ohio 45432

Received February 10, 2008; Revised Manuscript Received April 21, 2008

ABSTRACT: Microstructure evolution of a low hard segment (<10 mol %) thermoplastic polyurethane (LHS-TPU) has been followed by in-situ wide-angle X-ray (WAX) and small-angle X-ray scattering (SAX) with a focus on elucidating peculiar microstructural changes during uniaxial deformation ($\lambda = 1$ –3.5). For the LHS-TPU, the hard segments, due to their low content and chemical structure, do not crystallize but form glassy regions that act as physical cross-links. Two types of soft segment crystallites are resolved upon elongation via DSC, SAX, and WAX experiments. Phase I consists of a small amount of initial crystallites (<2%) that function similar to conventional PU hard segment domains, deforming at small uniaxial strains ($\lambda = 1$ –2) to a chevron-type morphology, which exhibit equatorial 4-point patterns in SAX. Phase II evolves at higher deformations ($\lambda > 2$) due to strain-induced crystallization. Phase II exhibits a conventional meridional 2-point pattern along the deformation direction with lamellar crystallites aligning in the plane normal to the deformation. WAX, SAX, and DSC confirm that both phases coexist over a small strain window ($\lambda = 1.9$ –2.5), demonstrating the independent nature of the two crystalline phases. These findings indicate that the LHS-TPU in this study is similar to poly(butylene adipate) (PBA) in its morphological and structural behavior. This is further substantiated by NMR, which reveals that the LHS-TPU consists of 90% soft segments, which are identified as PBA via crystal structure analysis of a highly aligned fiber. The soft segments in the LHS-TPU dominate the morphology and the X-ray patterns upon deformation.

I. Introduction

Thermoplastic polyurethane elastomers (TPUs) are made from diisocyanates and polyols containing an ester or ether backbone, which lead to linear segmented copolymers with alternating sequences of “hard” (diisocyanate) and “soft” (diols, diacids) segments. The microphase-separated morphology that results from the polarity difference of diol/diacid and diisocyanate segments leads to superior mechanical properties, such as higher strength, elongation, and modulus, with respect to other elastomers.¹ The unique mechanical behavior of TPUs is a major factor in their selection for many applications, ranging from medical devices² to deployable structures in space.³

Commonly the soft segments form amorphous regions that provide elastomeric behavior in combination with rigid elements such as chemical or physical cross-links. The hard segments form domains that consist of either glassy or semicrystalline regions that act as physical cross-links and provide stiffness and reinforcement. The reversibility of these regions enable melt processing at temperatures above the highest melting or glass transition temperature of the domains. The ability to combine a variety of different hard and soft segments provides broad flexibility to tailor secondary properties such as environmental stability and thermal expansion, while maintaining mechanical characteristics and processability. For example, the thermal expansion can be tailored via the amount of hard segments from elastomeric (soft) to thermoplastic (hard) behavior. The systematic development of a unique set of properties for a specific application, however, is based on an understanding of the correlation between molecular architecture, microphase-separated morphology, and the subsequent response of the microphase-separated domains to external perturbations such as strain. Recently, the addition of nanoparticles to

create “nanocomposites” has further extended the potential range of properties for materials, such as nanocomposite elastomers,⁴ conducting elastomers,⁵ and shape memory polymers.⁶ As with unfilled TPUs though, systematic exploitation of these opportunities is predicated upon expanding the established understanding of polymer architecture—morphology—strain relationships of neat TPUs to include the impact of the nanoparticle. Without the former, the latter is not possible.

One of the most effective characterization methods for molecular level morphology of polymeric systems and its evolution during external perturbations are X-ray techniques, including wide-angle X-ray diffraction (WAX) and small-angle X-ray scattering (SAX). An extensive number of investigations are available for neat polymers, such as poly(ethylene) (PE), poly(propylene) (PP), and other thermoplastics.^{7–11} These include detailed studies of polyurethanes (PU), both thermoplastic and thermoset, under uniaxial tension.^{12–14} The vast majority of the previous studies of PUs have examined the crystallinity of the hard segments and how variation in the hard segment content (>20 mol %) impacts the morphology. Additionally, these studies generally discuss the morphology before and after uniaxial deformation, lacking details associated with transient microstructures. In general, these scattering studies, along with other microscopy-based investigations of TPUs,¹⁵ indicate that domains containing hard segment crystallites are deformed at small uniaxial deformation due to local stress enhancement, arising from the modulus contrast between crystallite and amorphous surroundings. This is generally assumed to be the major source of irreversible deformation.¹ At higher elongations, hard segment crystallites fracture and rotate parallel to the major axis of deformation. In concert, the soft segments undergo strain-induced crystallization.

To complement the understanding of intermediate and high hard segment content TPUs, herein the uniaxial tensile deformation of a low hard segment TPU is followed by in-situ X-ray scattering using a synchrotron source. These studies are in support of the growing use of low hard segment TPUs as

* Corresponding author.

[†] AFRL/RXBP.

[‡] Universal Technology Corporation.

matrices for active nanocomposites, including shape memory materials⁶ and piezoresistive sensor elements.¹⁶ An unusual transition in SAX from an equatorial 4-point pattern to a meridional 2-point pattern is observed at low to intermediate strains. This reflects the superposition of response of two distinct soft segment crystalline regions to uniaxial deformation and is in contrast to previous observations in which hard segments govern the morphological changes.

II. Experimental Section

1. Sample Preparation. The neat thermoplastic polyurethane was supplied by Huntsman Polyurethanes (Irogran PS455-203, in the following referred to as Irogran). Samples were created via solution casting from THF (50 wt % THF solution, stirred for 8 h, cast into Teflon molds, and evaporated in hood for 24 h¹⁷). The samples were then dried in a vacuum oven at 50 °C until a constant weight was achieved. Samples may be produced in this manner whose lateral size approach several feet, with thickness from 0.5–2 mm. The molecular weight of Irogran was determined via an Agilent 1100 Series HPLC (solvent tetrahydrofuran and polystyrene as standard) as $M_w = 40K$ with a polydispersity of $PD = 2$.

2. Thermomechanical Characterization. Crystalline fraction and melting temperatures of samples were obtained using a TA Instruments DSC Q1000 with a heating/cooling rate of 4 °C/min, under an inert atmosphere. DMA measurements were carried out using a TA Instruments DMA 2980 with a temperature ramp of 4 °C/min on $4 \times 1 \times 10$ mm samples. Note for DSC and DMA the stretched samples reflect deformation that is relaxed to a zero stress state. In-situ X-ray reflects deformation under constant load. Thus, the extent of microscopic rearrangements of crystallites and polymer chains due to stress relaxation must be considered. Herein this relaxation is found not to impact the conclusions.

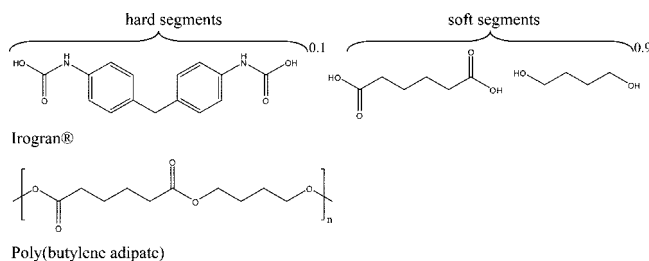
3. Small-Angle X-ray Scattering. Deformation–morphology correlations were determined using synchrotron X-ray experiments, conducted at X27C, National Synchrotron Light Source at Brookhaven National Laboratory. The sample-to-detector distance was 164 mm (WAX) and 1800 mm (SAX) at a wavelength of 0.1371 nm, defined by a double multilayer monochromator. The synchrotron X-rays were collimated to a 600 μ m beam size using a three-pinhole collimator.¹⁸ WAX and SAX images were obtained using a Mar CCD detector. $40 \times 4 \times 0.5$ mm samples were mounted in a modified Instron that allows uniaxial, symmetrical extension to expose the gauge section of the sample to the X-ray beam.

In-situ experiments were conducted at constant strain rates ($d\lambda/dt = 0.1$ –24 mm), and X-ray patterns were sequentially collected averaging over 25 s. This provided an elongation resolution of $\Delta\lambda = d\lambda/dt \times 25$ s. Note that the samples are deformed at room temperature and are always under an external load to maintain a symmetric elongation.

The X-ray data were initially corrected for background scattering, detector sensitivity, and variation of incident X-ray flux. Subsequent data reduction of the 2D X-ray patterns was carried out to obtain global average crystallinity of the sample by azimuthally averaging intensity vs 2θ using the software package Fit2D.¹⁹ An internal method was applied to determine the polymer crystallinity index as described in Alexander,⁷ which involves deconvolution of the 2θ data (amorphous and crystalline diffraction overlap). A more detailed explanation of this procedure is given in ref 20. In particular, the diffraction intensity is essentially a superposition of crystalline and amorphous intensities, I_c and I_a , respectively. The fraction crystallinity is then $X = I_c/(I_a + I_c)$. The diffraction pattern is circularly integrated. Peaks in a 2θ range between 10° and 30° are deconvoluted using Gaussian/Lorentzian peak fitting routines to give representative area fractions.

The Hermans orientation parameter was determined directly from 2-D X-ray data. A characteristic feature of X-ray patterns from a uniaxial oriented sample is the presence of arcs. The azimuthal width of the arcs provides information about the degree of the orientation of the respective scattering planes. The relative intensity

Scheme 1. Structure of Irogran According to NMR Measurements and Soft Segment Analogue Polyester Poly(butylene adipate)^a



^a The LHS-TPU Irogran contains 9.9% 4,4'-methylenediphenylene isocyanate (MDI), 58.2% butyl diol, and 31.8% adipate segments.

along the azimuth ($I(\varphi)$) at 2θ is related to the orientation distribution function (ODF) of the scattering planes. Approximating the ODF as a Legendre polynomial series in $\cos \varphi$, the Hermans orientation parameter S_d (or equivalently P_2) is the second moment average of the ODF and expressed as

$$S_d = \frac{3\langle \cos^2 \varphi \rangle - 1}{2} \quad (1)$$

For uniaxial orientation, S_d assumes values from -0.5 to 1 . -0.5 reflects perfect alignment in the plane perpendicular to the macroscopic elongation, 0 reflects random orientation, and 1 reflects perfect alignment along the uniaxial elongation.

Fast Fourier transformation of line schematics representing crystallite distribution were done with the public domain image analysis software ImageJ (<http://rsb.info.nih.gov/ij/>). The 2D patterns were subsequently refined via trial and error to match the intensity distribution of the experimental 2D SAX pattern.

X-ray fiber pattern simulation was carried out using Cerius² software package v4 (Accelrys) on a Silicon Graphics workstation. A standard force field was used to build a unit cell, and a minimization step was used before calculation of the 2D WAX pattern.

III. Results and Discussion

The LHS-TPU Irogran contains 9.9% 4,4'-methylenediphenylene isocyanate (MDI), 58.2% butyl diol, and 31.8% adipate segments⁵ (see Scheme 1). Previous proton NMR resolved the alkyl chain length and distribution of lengths of the diacid and diol segments, and the relative fraction of distinct protons indicates that the LHS-TPU contains $\sim 90\%$ diol/diacid soft segments. The polyester soft segments resemble the molecular structure of poly(butylene adipate) (PBA) (Scheme 1). Although the bisphenol A type aromatic hard segment (MDI) can be crystallized in some cases²¹ (hard segment content between 20 and 80%), it should favor amorphous hard domains at a content of only 10%.

The LHS-TPU exhibits two thermal transition regions (Figure 1a). The glass transition of amorphous soft domains ($T_{g,s} \sim -45$ °C) and melting of soft segment crystallites ($T_{m,s} \sim 35$ – 45 °C) occur at relatively low temperatures. This is consistent with the molecular structure of the soft segments, where PBA generally exhibits $T_g \sim -60$ °C and $T_m \sim 50$ – 55 °C.^{22,23} Additionally, lack of WAX features at temperatures greater than $T_{m,s}$ confirms that the molecular structure and low content of hard segments inhibit hard segment crystallization and result in amorphous hard segment domains (Figure 1b). The low content of these domains must contribute to the difficulty in resolving enthalpic features in DSC. Nevertheless, melt processability of Irogran at temperatures greater than 100 °C imply these hard segments soften at relatively low temperatures.⁶

The as-cast samples exhibit ~ 1 – 2% crystallinity (crystalline index, see Figure 4b) and an associated broad featureless

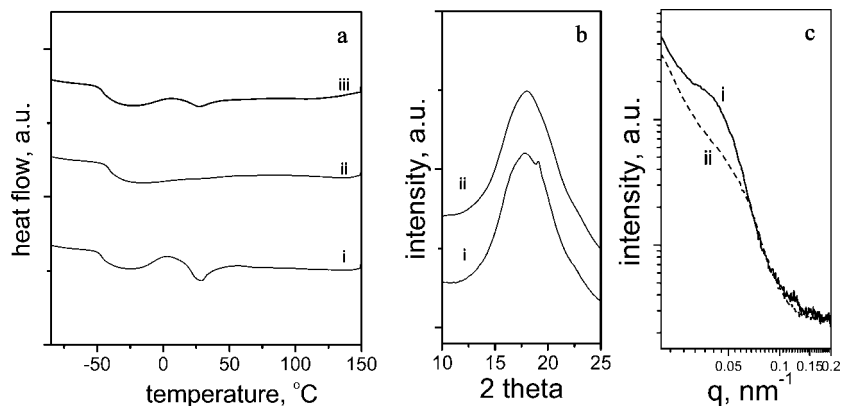


Figure 1. (a) Differential scanning calorimetry of neat Irogran. T_g at $-45\text{ }^{\circ}\text{C}$, melting peak of phase I at $30\text{ }^{\circ}\text{C}$. (i) As-cast sample, (ii) thermally erased sample, and (iii) 3 day room temperature annealed sample. (b) Wide-angle X-ray scattering comparing structure of the (i) as cast sample and (ii) thermally erased sample at $60\text{ }^{\circ}\text{C}$. (c) Small-angle X-ray scattering comparing crystallite structure of the (i) as-cast sample and (ii) thermally erased sample.

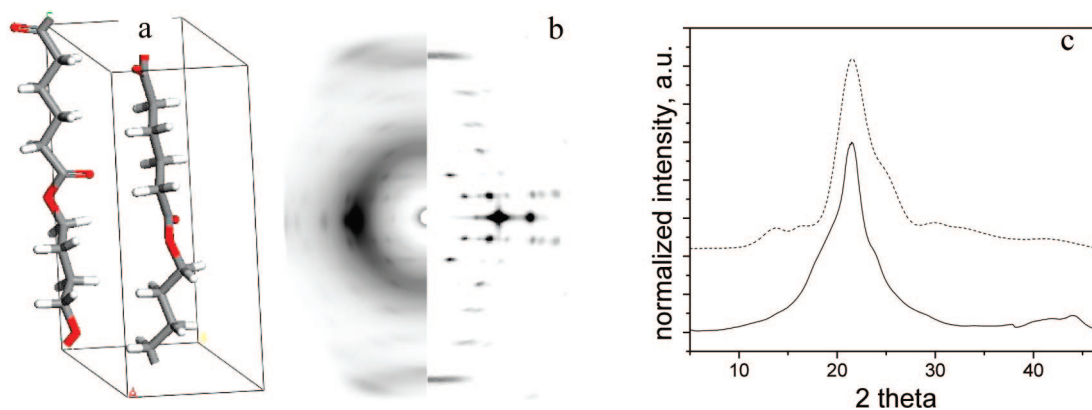


Figure 2. Probable crystal structure of Irogran: (a) unit cell with two poly(butylene adipate) chains constructed in Cerius²; (b) WAX fiber pattern of Irogran at $\lambda = 13$ with simulated 2D pattern from Cerius² overlaid; (c) simulated 2θ scan (dotted) compared to experimental data (solid).

endotherm at $\sim 30\text{ }^{\circ}\text{C}$ (Figure 1a, i). Thermal annealing at $T > T_{m,s}$ (e.g., $70\text{ }^{\circ}\text{C}$) erases these initial crystallites, and the resulting sample exhibits only a glass transition at $-45\text{ }^{\circ}\text{C}$ (Figure 1a, ii). SAX scattering of the as-cast sample (Figure 1c, i) and thermal annealed samples (Figure 1c, ii) confirms the disappearance of the initial crystallites. Very similar SAX patterns with peaks at 18 nm have been obtained for undeformed PBA at room temperature.²⁴ This verifies that the correlation feature in SAX for the as-cast film is not associated with density fluctuations between the amorphous hard segment domains but arises from the initial crystallites. The featureless SAX scattering after anneal in Figure 1c also implies that the microphase-separated morphology in this LHS-TPU does not exhibit a dominant length scale. Upon storage at ambient temperature for several days though, the 1–2% crystallinity returns (Figure 1a, iii). Note that a sample at room temperature is essentially annealed $70\text{ }^{\circ}\text{C}$ above its T_g and just $20\text{ }^{\circ}\text{C}$ below the soft segment melting point $T_{m,s}$; thus, physical aging is anticipated.

The neat LHS-TPU can be stretched up to 1200% ($\lambda = 13$) of its original length. At these elongations WAX shows a highly aligned fiber pattern that can be indexed to a monoclinic unit cell (Figure 2). Recall that the molecular structure of poly(butylene adipate) is isomeric (and likely isomorphic) to poly(ethylene suberate). Early studies²⁵ on thermoplastic polymers, such as poly(ethylene suberate), showed that to obtain high elongations of these polyesters, small amounts of diisocyanates were used in the polymerization reaction. This enhanced the elastomeric properties and thus provided the necessary elongation required to obtain good fiber patterns with sufficient data to derive the crystal structure of polymers such as poly(ethylene

suberate).⁸ The addition of small amounts of diisocyanates was also shown not to change the X-ray pattern but to improve sharpness and resolution of the crystalline diffraction pattern.

On the basis of the crystal structure of poly(ethylene suberate) and the isomeric chemical structure of PBA, a model was constructed in Cerius² (Figure 2a) and the fiber pattern calculated after energy minimization. There is good agreement between the observed and simulated fiber pattern (Figure 2b). The unit cell ($a = 5.51\text{ }\text{\AA}$, $b = 7.2\text{ }\text{\AA}$, $c \sim 14.4\text{ }\text{\AA}$, no registry along fiber axis) agrees well with the one obtained for PBA.²⁶

Similar to the β -phase discussed by Blackwell et al., the Irogran system does not exhibit registry along the fiber axis, likely due to the amorphous isocyanate units hindering perfect packing along this direction. Furthermore, the 20 prevalent diffraction peaks of Irogran's fiber pattern match those recently reported for the α -phase of PBA.²⁷ With the addition of line broadening parameters (e.g., crystallite size of $\sim 20\text{ nm}$), a 2θ simulation also shows good quantitative agreement with the scattering data (Figure 2c). Overall, the qualitative agreement between Irogran and PBA X-ray features implies that the observed crystalline diffraction peaks in WAX arise exclusively from the soft segments.

1. Microstructure–Deformation Correlation. Figure 3 summarizes data obtained from fitting in-situ scattering from the room temperature deformation of the LHS-TPU (see Experimental Section for details on data analysis). The stress–strain response exhibits typical behavior of elastomers with an initial elastic response followed by yielding, typically around $\lambda = 1.3$ (point 1). Further elongation leads to strain

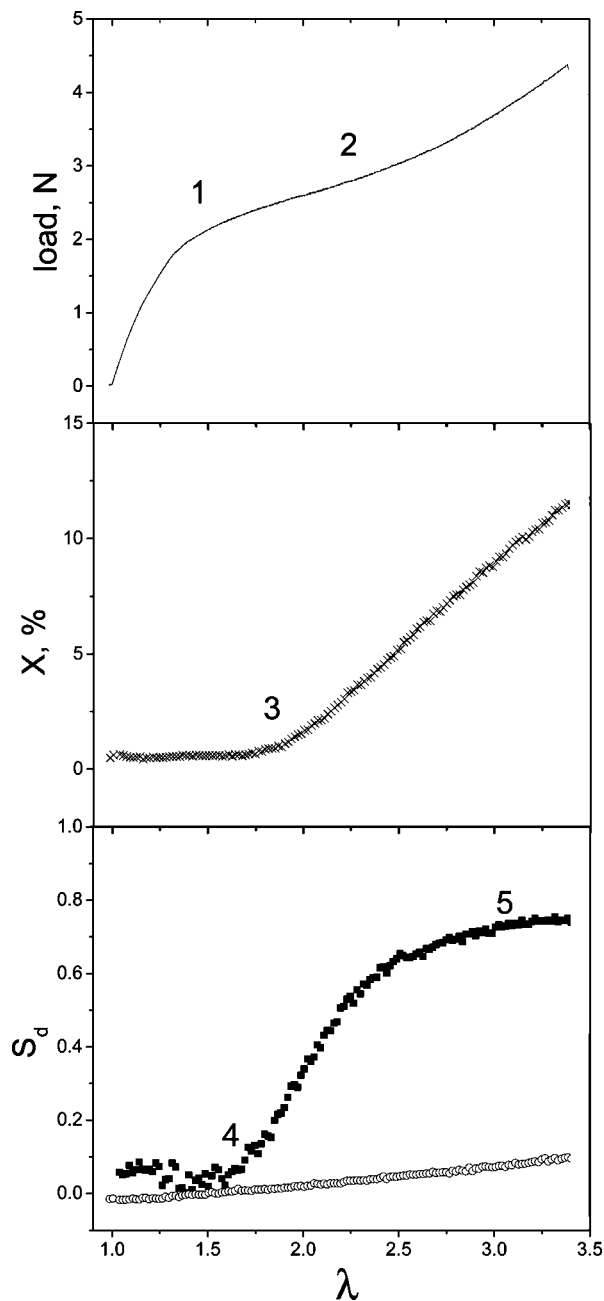


Figure 3. Summary of in-situ deformation-WAX study. Elongation was performed at 1 mm/min (solid line). X-ray pattern analysis provide orientation parameter S_d of soft segment crystallites (●) and amorphous regions (○) as well as the crystallinity index (fraction), X (×). Characteristic points include (1) yield, (2) onset of strain hardening, (3) onset of strain-induced crystallization, (4) onset of crystallite alignment, and (5) plateau of crystallite alignment.

hardening, noticeable by an increase in stress between $\lambda = 2$ – 2.5 (point 2). Beyond this stage, the system exhibits a quasi-linear increase in stress with further deformation until it ruptures at $\lambda_{\text{failure}} \sim 10$ – 13 .

Overall, the in-situ X-ray measurements confirm that the LHS-TPU undergoes strain-induced crystallization. The amorphous regions exhibit a linear increase in order with strain, reflecting the entropic distortion of the amorphous chain conformations. After yielding and slightly before strain hardening ($\lambda \sim 2$, point 3), the crystallinity index linearly increases to intermediate strains ($X \sim 13\%$, $\lambda = 3.5$). Beyond deformations of $\lambda \sim 8$, the incremental increase in crystallinity index with additional strain decreases, reaching up to 50% in a fully stretched sample, $\lambda = 13$.⁵ In conjunction, the soft segment

crystallites (initial and strain induced) begin to orient after yielding (point 4), reaching a maximum degree of uniaxial orientation shortly after strain hardening begins (point 5).

Figure 4 summarizes DSC studies for $\lambda = 1$ to $\lambda = 5$, complementing in-situ X-ray experiments. Overall, the enthalpy of the endotherm associated with melting of soft segment crystallites increases with increasing strain. The enthalpy change between 35 and 45 °C (Figure 4a,b) exhibits a marked upturn around $\lambda = 1.5$ – 2 , in excellent agreement with the noticeable upturn in crystallinity index observed in WAX (Figure 3). The % crystallinity from DSC in Figure 4b was estimated via enthalpy data of a fully crystallized PBA sample²² (60 J/g), with a correction of 0.9 (90% soft segment). The % crystallinity index from WAX is slightly smaller since crystalline contributions outside the finite 2θ window ($2\theta = 13^\circ$ – 26°) were neglected. The narrowing of the melting peak and minor shift to higher temperatures in Figure 4a ($\Delta 2^\circ\text{C}$) indicates an increase in primary crystallite size and better order within crystallites. This is not consistent with breakup of hard segment crystallites as reported for conventional polyurethanes and further confirms the soft segment dominance in the LHS-TPU.

The increased content of these strain-induced crystallites is also reflected in the increased mechanical properties (Figure 5). Up to the melting of the soft segment crystallites the storage modulus of a prestretched sample ($\lambda = 5$) is increased by a factor of 4 over the original sample ($\lambda = 1$) due to the nanoscale reinforcement provided by microphase-separated soft segment crystallites. Note that once the soft segments melt ($>40^\circ\text{C}$), the sample flows, and reliable dynamic modulus data were not available.

Careful examination of the DSC traces, however, implies that there is more than one form of the soft segment crystallites. With increased elongation, the DSC features appear to reflect two distinct events: an initial broad endotherm reflecting 1–2% equilibrium crystallites (I) with the addition of a narrow endotherm at 40 °C (II) at higher elongations (Figure 4). For deformation of $\lambda = 1.5$, both peaks are visible. The initial broad endotherm at lower temperatures (I) disappears at elongations $\lambda > 2.5$. The occurrence of two melting endotherms (phases) in the early stages of elongation implies that this LHS-TPU may exhibit similar polymorphic behavior as PBA. Previous characterization of poly(butylene adipate)²⁶ via DSC and X-ray indicate PBA exhibits two crystalline polymorphs α and β , with the α phase being the preferred stable phase.²⁸

2. Crystallite Orientation with Deformation. 2D SAX and WAX at low strain reveals additional complexity to the development of crystallites in this LHS-TPU. Figures 6 (2D patterns), 7a (WAX scan), and 7b (azimuthal SAX) summarize the evolution of the anisotropic SAX and WAX scattering with deformation. To aid the visualization of the crystallite distribution, hypothesized morphologies are shown alongside the 2D SAX and WAX data (Figure 6, column 1). Line groups are used to represent collections of parallel lamellae. Owing to the uniaxial symmetry of the experimental setup, fast Fourier transformation (FFT) of the simplistic line patterns can be compared directly to the 2D intensity distribution in the small angle region (Figure 6, columns 2 and 3). It is important to note that it is not directly possible to reveal whether the SAX pattern is caused by homogeneously dispersed individual crystallites or islands of crystallite-rich regions (spherulites) in an amorphous matrix. The crystallite distribution in the schematic thus is intended to only reflect the relative orientation distribution and not imply relative crystallite–crystallite distance or arrangement.

At $\lambda = 1$, a uniform ring at $d \sim 18$ nm indicates an isotropic arrangement of the initial small amount of crystallites (Figures 6a and 7a). At small elongations ($1 < \lambda < 1.3$), the ring deforms

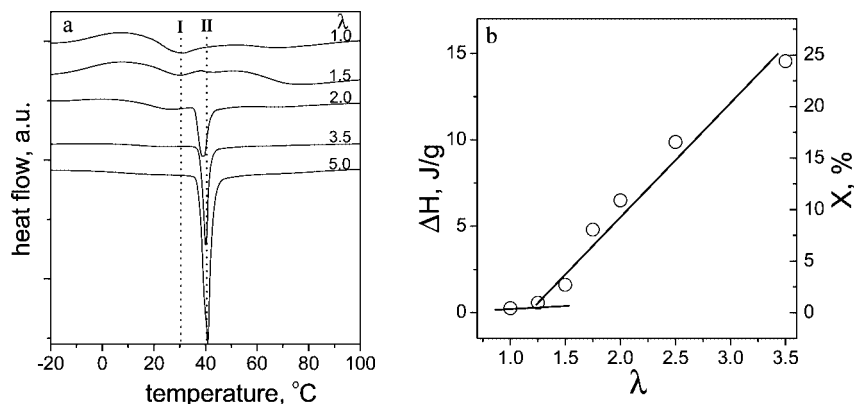


Figure 4. (a) DSC traces for PU at different elongations. Melting peak of phase I at ~ 30 °C and melting peak of phase II at 40 °C. (b) Melting enthalpies of phase II obtained from DSC measurements of strained Irogran samples.

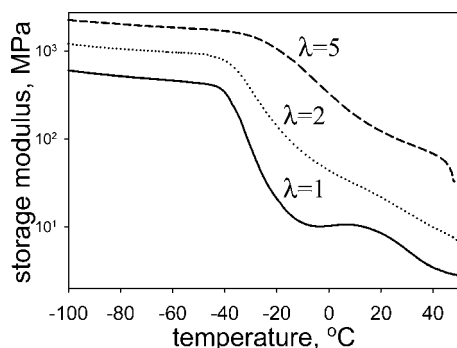


Figure 5. Storage modulus (DMA) of stretched Irogran samples.

to an ellipsoid with the long dimension on the equator (Figure 6b). This can be explained by a slight expansion of the crystallite long period along the stretching direction and a simultaneous contraction perpendicularly. WAX data (Figure 6b) show a broad amorphous peak at $2\theta = 20^\circ$ with a small narrow diffraction peak toward larger angles ($2\theta = 22^\circ$). A radial line scan of the WAX (Figure 7a) shows that the intensity distributions on the meridian and equator are identical, confirming isotropic arrangement of the scattering objects and negating the possibility that the change in SAX features arise from crystallite reorientation.

At elongations between $\lambda = 1.3$ and 1.9, a 4-point SAX pattern develops (Figure 6c). An excellent summary on the origins of 4-point patterns is given by Murthy and Grubb.²⁹ These features result from interlamellar shear at the microdomain level, leading to chevron-type crystallite arrangements. Sometimes, weak scattering intensity on the equator combines the lobes of the 4-point peaks, leading to the appearance of a figure eight pattern. This is the case for Irogran. Figure eight patterns have also been described in some detail by Tsvankin et al.³⁰ and by Hsiao et al.³¹ Mahendresingam et al.^{13,32} reported strikingly similar SAX patterns to those discussed here (up to $\lambda = 1.9$ in this study) in their PU system, with a change from an isotropic ring to an equatorial 4-point pattern at $\lambda = 1.5$. Furthermore, in-situ studies by Yeh et al. show similarities to the SAX observations, although the contrast mechanism is explained by changes in hard segment morphology.³³ The transition from Figure 6b to Figure 6c can be simulated in the schematic with small changes in the outer columns as well as changes of the middle rows, which dominate the scattering changes. The distance between lines within the columns are closer from Figure 6b to Figure 6c where rows are aligned along the deformation direction in addition to slight rotation.

Accompanying the SAX pattern development from $\lambda = 1.3$ to 1.9, WAX shows alignment of the 013 diffraction peak on

the meridian. Note that the later developing 110 peak is located at the same 2θ angle but with much sharper and higher in intensity than the 013. Only by following the intensity of the 013 in real time and 2D is it possible to distinguish it from the 110 peak. The lattice plane causing this diffraction peak is perpendicular to the later developing strong 110 peak on the equator. A 2θ scan along the meridian shows a small reflection at 0.45 nm on top of the broad amorphous peak, whereas the equatorial scan exhibits a reflection of lower intensity (Figure 7a, $\lambda = 1.3$). The meridional placement of the (013) reflection is in agreement with indexing of tilted chevron-type crystallites in accordance with the line schematic in Figure 6c.

Additional deformation beyond $\lambda = 1.9$ transforms the 4-point to a butterfly pattern (Figure 6d).²⁹ At the same time a meridional streak develops close to the beamstop (Figure 6d), which turns into a new scattering maximum on the meridian upon further elongation ($\lambda > 2.0$). The coexistence of the meridional streak and the 4-point pattern can be seen in Figure 7b at $\lambda = 1.75/1.9$, at which point a total of six maxima (4 + 2) are present in the azimuthal scan. The emergence of the latter two maxima begins around $\lambda = 1.75$, in agreement with the onset of strain-induced crystallization of the soft segments. Also, WAX clearly shows a new sharp peak developing on the equator (Figures 6d and 7a). The appearance of this new peak and the SAX streak can be explained by the superposition of already existing chevron-type crystallites and newly formed crystallites (red in Figure 6d) with lamellae oriented perpendicular and polymer chains parallel to the elongation direction.

Similar observations of six maxima from static SAX experiments on PE have been ascribed to rearrangement of crystallites, without the formation of new crystallites. For example, Tsvankin et al. describe their finding in stretched PE samples as a transformation of a lamellar to a fibrillar morphology.³⁰ For the LHS-TPU Irogran, however, the combination of SAX and WAX with DSC shows that there are two distinct, independent types of crystallites: (I) chevron-type morphology due to microdomain shear of already existing spherulite-like crystallites ($< 2\%$) and (II) the appearance of new strain-induced crystallites with a uniaxial orientation. The coexistence of both phases over a range of deformation ($\lambda \sim 1.9$ –2.2) favors the supposition that phase II emerges from the amorphous domains and not from a direct conversion of I into II. The role of phase I or existing hard segment domains in templating or nucleating the development of phase II crystallites is not known, but local strain enhancement near these relatively rigid domains should enhance chain alignment, favoring strain-induced soft segment crystallization. It is also feasible that row-nucleated crystallization takes place as observed by Olley et al. in shear-enhanced crystallization of poly(propylene).³⁴ In this case a fibrillar morphology of either hard segments or soft segment crystallites along the deformation

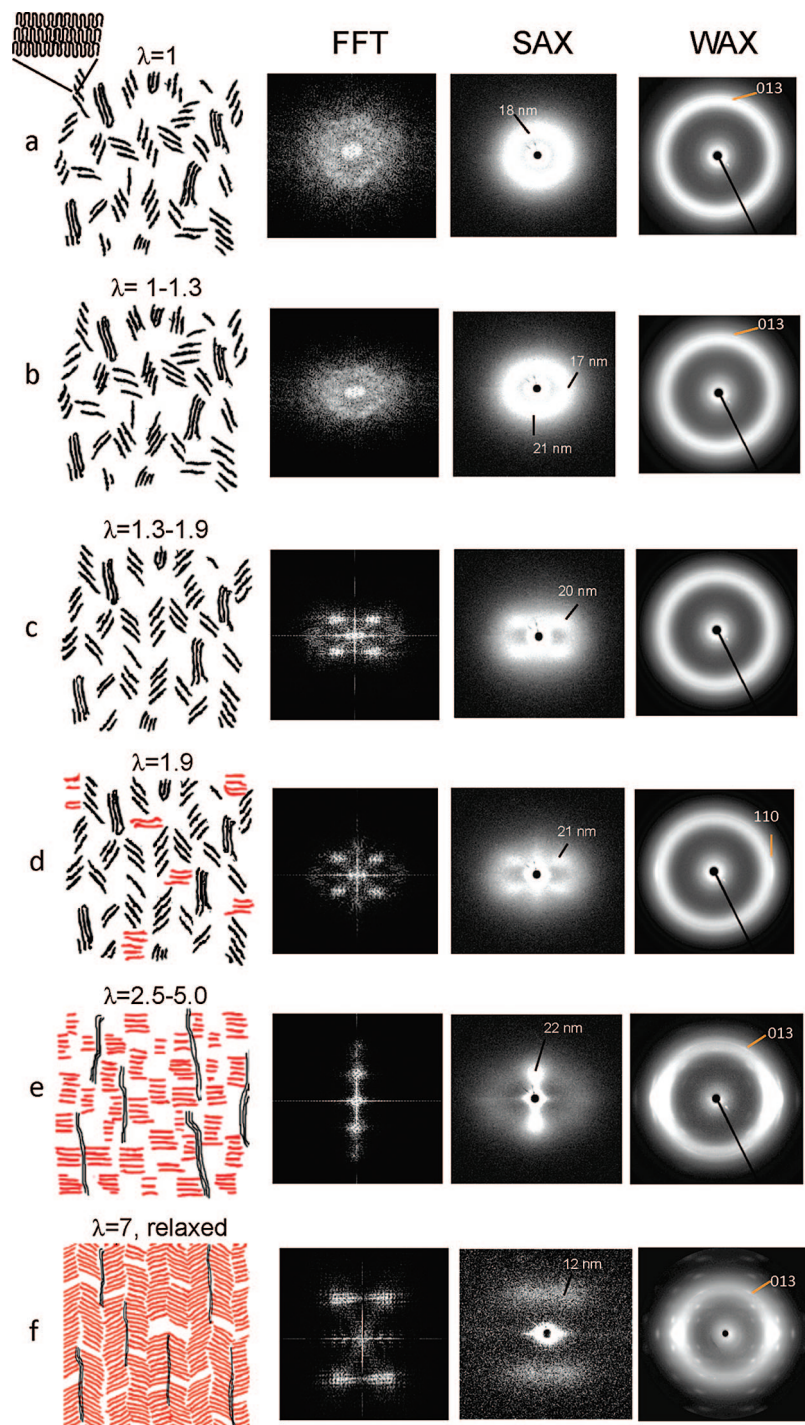


Figure 6. Wide-angle (column 4) and small-angle X-ray (column 3) patterns of neat PU upon deformation and schematic representation (column 1) of morphology with fast Fourier transformation (column 2): (a) undeformed; (b) small strains, $\lambda = 1-1.3$; (c) intermediate strains, $\lambda = 1.3-1.9$; (d) transient structure, $\lambda = 1.9$; (e) large strains, $\lambda = 2.5-5$; (f) relaxed from large strains ($\lambda = 7$).

may locally enhance the formation of a lamellar morphology of new soft segments crystallites. It is important to note that the transition from a 4-point to an orthogonal 2-point pattern observed for Irogran is different from the commonly observed 2-point to 4-point transition observed for a number of thermoplastic materials. In these latter cases, a meridional 2-point changes into a meridional 4-point or vice versa,³⁵ reflecting a fracture or slippage of crystallites.

Upon further deformation, the 4-point pattern is completely replaced by the conventional meridional 2-point pattern (Figure 6e). The d -spacing of the meridional lamellar peak decreases from 22 nm at $\lambda \sim 2.0$ to 12 nm at elongations $\lambda > 7.0$. The reduction in crystallite long period is in agreement with NMR

data.³⁶ Higher elongations lead to smearing of this peak equatorially. This reflects undulations of the lamellae perpendicular to the stretching direction due to lateral compression on the edges of the crystallites associated with the Poisson effect.

Furthermore, the different orientations in Figure 6d are a natural consequence of some regions being under different stress, including some under very low stress, while in Figure 6e all have seen somewhat higher stresses even though it is still heterogeneous (highest where the fibrils are), and the fibrils cause the streak in the SAX pattern of Figure 6e.

The appearance of the meridional two-point pattern in Figure 6d is accompanied by a new diffraction peak (110) that emerges on the equator in WAX. The (110) intensity increases as

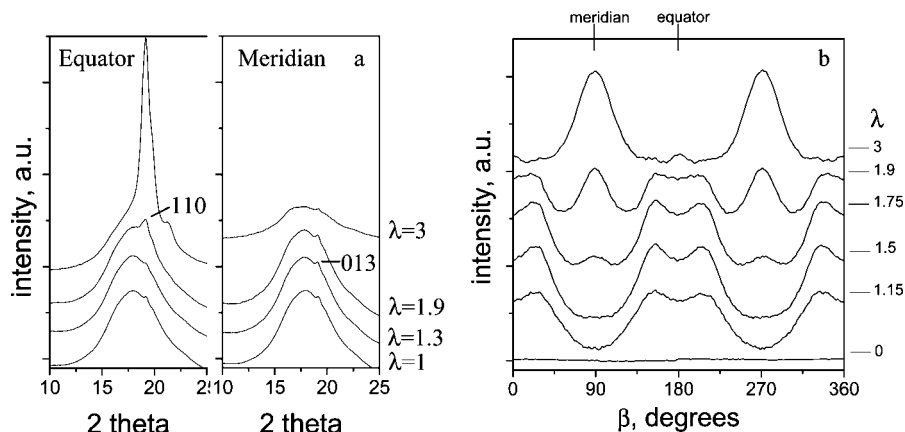


Figure 7. (a) WAX 2θ scans of Irogran at different elongations: equatorial scan (perpendicular to uniaxial stretch) and meridional scan (parallel to uniaxial stretch). (b) Azimuthal intensity distribution for Irogran at different elongations at 18 nm peak ($q = 0.04 \text{ \AA}^{-1}$).

elongation proceeds (Figure 7a). Consistent with the meridional SAX reflection, the 013 reflection of the new soft segment crystallites develops into a layer line with two distinct diffraction peaks at higher elongations (Figure 6e). The fact that the 013 diffraction peak position from the initial chevron morphology and the new crystalline phase emerging upon elongation is identical suggests that the unit cell of these two crystalline phases is very similar (similar to α and β phase of PBA²⁶).

Finally, unloading of the polymer from $\lambda > 9$ to an unloaded state leads to a 4-point pattern, as shown in Figure 6f. This behavior is typically observed for cold drawn poly(ethylene)³⁷ and is interpreted as chevron-type tilts of crystallites due to local strain relaxation. Note that this tilt is not equivalent to the tilt at initial elongations. The tilt is meridional and much smaller. In addition, the SAX pattern shows a strong equatorial streak, which is common for polymers at high elongations due to crazing, void formation, which have been reported for this system,⁵ or row nucleated crystallites.³⁴

IV. Summary

In conclusion, results from X-ray experiments show that the neat LHS-TPU system shows a transient morphology at low strains, dominated by soft segments crystallites, involving the coexistence of two independent crystalline phases. A small amount of crystallites present in the as-made sample (phase I) leads to a chevron-type morphology upon small deformations ($\lambda < 2$), with the appearance of an equatorial figure eight pattern in SAX. Further stretching of the sample leads to new crystallites (phase II) that exhibit typical lamellar morphology with crystallites perpendicular to the stretching direction. Our current understanding of the origins for the initial crystalline phase is that the inherent polymorphism of the underlying poly(butylene adipate) structure (90%) and the presence of amorphous hard segment domains is nucleating phase I. Phase II is developing upon larger strains and exhibits structural parameters that are very similar to the α -phase of PBA. The low content of hard segments in the Irogran system does not dominate in the room temperature characteristics and at most are a cocontributor to the observed soft segment morphology. The subsequent mechanical properties are ultimately associated with these soft segment crystallites, which differentiates LHS-TPUs from conventionally used TPUs with larger amounts of hard segments. When exploiting LHS-TPUs for nanocomposite design, it is imperative to realize that the soft segments are the major factor in interactions with particular nanoparticulates, such as carbon nanotubes.

Acknowledgment. The authors acknowledge funding from the Air Force Office of Scientific Research as well as the Air Force

Research Laboratory and the AFRL Materials and Manufacturing Directorate. J.K. was funded by SOCHE. We thank Marlene Houtz for help with DMA and DSC measurements and Lawrence Drummy and Michael Arlen for help with Synchrotron data collection. We further thank Lixia Rong at beamline X27C of the National Synchrotron Light Source at Brookhaven for help with the in-situ X-ray experiments and Peter Mirau for in depth NMR characterization of the polymer.

References and Notes

- (1) Curgul, S.; Yilgor, I.; Yilgor, E.; Erman, B.; Cakmak, M. *Macromolecules* **2004**, *37*, 8676–8685.
- (2) Lendlein, A.; Kelch, S. *Angew. Chem., Int. Ed.* **2002**, *41*, 2034–2057.
- (3) Sokolowski, W.; Chmielewski, A.; Hayashi, S.; Yamada, T. Colder hibernated elastic memory (CHEM) self-deployable structures. Proceeding of the SPIE International Symposium on Smart Structures and Materials, Newport Beach, CA, March 1–5, **1999**; Vol. 3669, pp 179–185.
- (4) Alexandre, M.; Dubois, P. *Mater. Sci. Eng., R* **2000**, *28*, 1–63.
- (5) Koerner, H.; Liu, W.; Alexander, M.; Mirau, P.; Dowty, H.; Vaia, R. *Polymer* **2005**, *46*, 4405–4420.
- (6) Koerner, H.; Price, G.; Pearce, N. A.; Alexander, M.; Vaia, R. A. *Nat. Mater.* **2004**, *3*, 115–120.
- (7) Alexander, L. E. *X-Ray Diffraction Methods in Polymer Science*; Wiley-Interscience: New York, 1970.
- (8) Kakudo, M.; Kasai, N. *X-ray Diffraction by Polymers*; Kodansha: Tokyo, 1972.
- (9) Keum, J. K.; Somani, R. H.; Zuo, F.; Burger, C.; Sics, I.; Hsiao, B. S.; Chen, H.; Kolb, R.; Lue, C.-T. *Macromolecules* **2005**, *38*, 5128–5136.
- (10) Kumaraswamy, G.; Verma, R. K.; Kornfield, J. A.; Yeh, F.; Hsiao, B. S. *Macromolecules* **2005**, *37*, 9005–9017.
- (11) Stribeck, N.; Funari, S. S. *J. Polym. Sci., Part B: Polym. Phys.* **2003**, *41*, 1947–1954.
- (12) Laity, P. R.; Taylor, J. E.; Wong, S. S.; Khunkamchoo, P.; Norris, K.; Cable, M.; Andrews, G. T.; Johnson, A. F.; Cameron, R. E. *Polymer* **2004**, *45*, 5215–5232.
- (13) Blundell, D. J.; Eeckhaut, G.; Fuller, W.; Mahendrasingam, A.; Martin, C. J. *Macromol. Sci., Phys.* **2004**, *B43*, 125–142.
- (14) Desper, C. R.; Schneider, N. S.; Jasinski, J. P.; Lin, J. S. *Macromolecules* **1985**, *18*, 2755–2761.
- (15) (a) McLean, R. S.; Sauer, B. B. *J. Polym. Sci., Part B: Polym. Phys.* **1999**, *37*, 859–866. (b) Sauer, B. B.; McLean, R. S.; Brill, D. J.; Londono, D. J. *J. Polym. Sci., Part B: Polym. Phys.* **2002**, *40*, 1727–1740.
- (16) Engel, J.; Chen, J.; Liu, C.; Bullen, D. Polyurethane Rubber All-Polymer Artificial Hair Cell Sensor. *IEEE/ASME J. MEMS* **2006**.
- (17) US Patent # 6,680,016.
- (18) Fu, B. X.; Hsiao, B. S.; Pagola, S.; Stephens, P.; White, H.; Rafailovich, M.; Sokolov, J.; Mather, P. T.; Jeon, H. G.; Phillips, S.; Lichtenhan, J.; Schwab, J. *Polymer* **2001**, *42*, 599–611.
- (19) (a) Hammersley, A. P. ESRF Internal Report ESRF97HA02F, “Fit2D: An Introduction and Overview, **1997**. (b) Hammersley, A. P.; Svensson, S. O.; Hanfland, M.; Fitch, A. N.; Haeusermann, D. *High Pressure Res.* **1996**, *14*, 235–248.
- (20) Koerner, H.; Lui, Y.; Li, X.; Cohen, C.; Hedden, R. C.; Ober, C. K. *Macromolecules* **2003**, *36*, 19751981.3.
- (21) Lamba, N. M. K.; Woodhouse, K. A.; Cooper, S. L. *Polyurethanes in Biomedical Applications*; CRC Press: Boca Raton, FL, 1998; p 64.

- (22) Zhao, L.; Wang, X.; Li, L.; Gan, Z. *Polymer* **2007**, *48*, 6152–6161.
- (23) Gan, Z.; Abe, H.; Doi, Y. *Macromol. Chem. Phys.* **2002**, *203*, 2369–2374.
- (24) Gan, Z.; Kuwabara, K.; Abe, H.; Iwata, T.; Doi, Y. *Biomacromolecules* **2004**, *5*, 371–378.
- (25) Turner-Jones, A.; Bunn, C. W. *Acta Crystallogr.* **1962**, *15*, 105–113.
- (26) (a) Minke, R.; Blackwell, J. J. *Macromol. Sci., Phys.* **1979**, *B16*, 407–17. (b) Minke, R.; Blackwell, J. J. *Macromol. Sci., Phys.* **1980**, *B18*, 233–55.
- (27) Noguchi, K.; Kondo, H.; Ichikawa, Y.; Okuyama, K.; Washiyama, J. *Polymer* **2005**, *46*, 10823–108.
- (28) Kai, W.; Zhu, B.; He, Y.; Inoue, Y. *J. Polym. Sci., Part B: Polym. Phys.* **2005**, *43*, 2340–2351.
- (29) (a) Wang, W.; Murthy, N. S.; Grubb, D. T. *Polymer* **2007**, *48*, 3393–3399. (b) Murthy, N. S.; Grubb, D. T.; Zero, K. *Macromolecules* **2000**, *33*, 1012–1021.
- (30) Gerasimov, V. I.; Genin, Ya, V.; Tsvankin, D. Ya. *J. Polym. Sci., Part B: Polym. Phys. Ed.* **1974**, *12*, 2035–46.
- (31) Chen, X.; Yoon, K.; Burger, C.; Sics, I.; Fang, D.; Hsiao, B.; Chu, B. *Macromolecules* **2005**, *38*, 3883–3893.
- (32) Blundell, D. J.; Eeckhaut, G.; Fuller, W.; Mahendrasingam, A.; Martin, C. *Polymer* **2002**, *43*, 5197–5207.
- (33) Yeh, F.; Hsiao, B. S.; Sauer, B. B.; Michel, S.; Siesler, H. W. *Macromolecules* **2004**, *36*, 1940–1954.
- (34) Kumaraswamy, G.; Verma, R. K.; Issaian, A. M.; Wang, P.; Kornfield, J. A.; Yeh, F.; Hsiao, B. S.; Olley, R. H. *Polymer* **2000**, *41*, 8931–8940.
- (35) Murthy, N. S.; Grubb, D. T. *J. Polym. Sci., Part B: Polym. Phys. Ed.* **2002**, *40*, 691–705.
- (36) Powers, D.; Mirau, P.; Koerner, H.; Vaia, R. *Macromolecules*, accepted.
- (37) Belbeoch, B.; Guinier, A. *Makromol. Chem.* **1951**, *31*, 1.

MA800306Z